Bone cell response to additively manufactured 3D micro-architectures with controlled Poisson's ratio
Auxetic vs. non-auxetic meta-biomaterials

Yarali, Ebrahim; Klimopoulou, Maria; David, Kristen; Boukany, Pouyan E.; Staufer, Urs; Fratila-Apachitei, Lidy E.; Zadpoor, Amir A.; Accardo, Angelo; Mirzaali, Mohammad J.

Important note
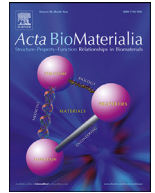To cite this publication, please use the final published version (if applicable).
Please check the document version above.

Full length article

Bone cell response to additively manufactured 3D micro-architectures with controlled Poisson's ratio: Auxetic *vs.* non-auxetic meta-biomaterials

Ebrahim Yarali [a,b,*], Maria Klimopoulou [a], Kristen David [c], Pouyan E. Boukany [c], Urs Staufer [b], Lidy E. Fratila-Apachitei [a], Amir A. Zadpoor [a], Angelo Accardo [b,1,*], Mohammad J. Mirzaali [a,1,*]

[a] Department of Biomechanical Engineering, Faculty of Mechanical Engineering, Delft University of Technology, Mekelweg 2, 2628 CD, Delft, The Netherlands
[b] Department of Precision and Microsystems Engineering, Faculty of Mechanical Engineering, Delft University of Technology, Mekelweg 2, 2628 CD, Delft, The Netherlands
[c] Department of Chemical Engineering, Faculty of Applied Sciences, Delft University of Technology, Van der Maasweg 9, 2629 HZ, Delft, The Netherlands

ARTICLE INFO

ABSTRACT

The Poisson's ratio and elastic modulus are two parameters determining the elastic behavior of biomaterials. While the effects of elastic modulus on the cell response is widely studied, very little is known regarding the effects of the Poisson's ratio. The micro-architecture of meta-biomaterials determines not only the Poisson's ratio but also several other parameters that also influence cell response, such as porosity, pore size, and effective elastic modulus. It is, therefore, very challenging to isolate the effects of the Poisson's ratio from those of other micro-architectural parameters. Here, we computationally design meta-biomaterials with controlled Poisson's ratios, ranging between -0.74 and +0.74, while maintaining consistent porosity, pore size, and effective elastic modulus. The 3D meta-biomaterials were additively manufactured at the micro-scale using two-photon polymerization (2PP), and were mechanically evaluated at the meso–scale. The response of murine preosteoblasts to these meta-biomaterials was then studied using *in vitro* cell culture models. Meta-biomaterials with positive Poisson's ratios resulted in higher metabolic activity than those with negative values. The cells could attach and infiltrate all meta-biomaterials from the bottom to the top, fully covering the scaffolds after 17 days of culture. Interestingly, the meta-biomaterials exhibited different cell-induced deformations (*e.g.,* shrinkage or local bending) as observed via scanning electron microscopy. The outcomes of osteogenic differentiation (*i.e.,* Runx2 immunofluorescent staining) and matrix mineralization (*i.e.,* Alizarin red staining) assays indicated the significant potential impact of these meta-biomaterials in the field of bone tissue engineering, paving the way for the development of advanced bone meta-implants.

Statement of significance

We studied the influence of Poisson's ratio on bone cell response in meta-biomaterials. While elastic modulus effects are well-studied, the impact of Poisson's ratio, especially negative values found in architected biomaterials, remains largely unexplored. The complexity arises from intertwined micro-architectural parameters, such as porosity and elastic modulus, making it challenging to isolate the Poisson's ratio. To overcome this limitation, this study employed rational computational design to create meta-biomaterials with controlled Poisson's ratios, alongside consistent effective elastic modulus, porosity, and pore size. The study reveals that two-photon polymerized 3D meta-biomaterials with positive Poisson's ratios displayed higher metabolic activity, while all the developed meta-biomaterials supported

* Corresponding authors.
E-mail addresses: E.yarali@tudelft.nl (E. Yarali), A.Accardo@tudelft.nl (A. Accardo), M.J.Mirzaali@tudelft.nl (M.J. Mirzaali).
[1] These authors jointly supervised this work.

osteogenic differentiation of preosteoblasts as well as matrix mineralization. The outcomes pave the way for the development of advanced 3D bone tissue models and meta-implants.

1. Introduction

Both the effective elastic modulus of the scaffolds (∼stiffness) and the biomaterial's Young modulus may modulate cell fate and subsequent tissue development through mechanotransduction pathways involving cytoskeletal reorganization, and changes in gene expression and protein synthesis [1–4]. It is, therefore, necessary to consider the elastic modulus of the target tissue in the design of biomaterials and scaffolds, which can vary greatly from soft tissues (*e.g.,* brain with an elastic modulus of approximately 1–4 kPa [5–7]) to hard tissues (*e.g.,* cancellous bone with an elastic modulus in the range of 0.04–1 GPa [6,8]).

Several strategies can be employed to modulate the effective elastic modulus of scaffolds depending on the targeted tissue, biochemical properties, and manufacturing techniques. These strategies encompass a variety of factors, including the base material, coating, external stimuli, and geometrical cues [9–11]. For instance, in porous scaffolds or implants, the micro-architectural design determines the effective elastic modulus with porosity and pore size serving as critical morphological parameters that need to be tailored to mimic native tissues [12,13].

In addition to the effective elastic modulus, the Poisson's ratio (*i.e.,* the negative ratio of the transverse to the longitudinal strain) is a crucial factor in biomaterial design and is known to play a significant role in regulating cell behavior [9,14–17]. The Poisson's ratio of architected biomaterials with repetitive unit cells is a function of the kinematic design of their underlying mechanisms. This ratio can be varied from negative to positive values by rationally adjusting the geometrical designs of the repetitive unit cells [18,19]. Mechanical metamaterials offer a promising approach to control the Poisson's ratio while keeping the effective elastic modulus unaffected. These materials are a class of advanced engineered materials featuring unconventional properties owing to their micro-architectural design [20–27].

One example of the unusual properties of mechanical metamaterials is the auxetic property or negative Poisson's ratio. Auxetic metamaterials expand transversely when stretched longitudinally and contract transversely when compressed longitudinally, which is the opposite of the behavior shown by conventional materials [20,28–31]. This unique property can make auxetic materials ideal for use in hybrid hip implants, as they can expand on the side of the implant experiencing tension under bending [32]. This can solve the current challenges in traditional hip implants which exhibit shrinkage on the tension side and expansion on the compression side under such loading conditions. Expansion on the compression side is beneficial as it promotes adherence to the surrounding bone and prevents aseptic loosening. However, the shrinkage on the tension side may eventually lead to the creation of a gap between the bone and the implant, increasing the risk of implant loosening. Auxetic meta-biomaterials could address this problem by offering a negative Poisson's ratio on the tension side of such implants, which has been already demonstrated as a conceptual design and early prototype [32]. Such a design, therefore, can prevent implant loosening and improve the connection between the implant and the surrounding bone [32,33]. Therefore, auxetic meta-biomaterials have the potential to offer unique solutions to the challenges faced in the design of implantable medical devices [34].

To better understand the effects of mechanical cues on cell-scaffold interactions, both effective elastic modulus and Poisson's ratio must be considered. However, the maximum values of both the Poisson's ratio and effective elastic modulus are coupled with each other (Hashin–Shtrikman bounds [35–37]). The effective elastic modulus is coupled with micro-architectural parameters, which makes it challenging to change either the morphology or the elastic behavior without affecting the other. However, rational design techniques could be used to decouple the Poisson's ratio of meta-biomaterials from their effective elastic modulus and morphological properties.

Recent studies have highlighted the significance of the Poisson's ratio in regulating cell behavior [9,13,17,38–40]. For example, negative values of the Poisson's ratio have been shown to differently affect cell proliferation [17], differentiation [9], alignment, and directionality, as compared to positive values of the Poisson's ratio [16]. However, most research has focused on the effect of the Poisson's ratio in 2D (and 2.5D) meta-biomaterials, with only a few studies investigating the impact of the Poisson's ratio in 3D biomaterials [9,16,40]. In those studies, however, the interdependence between micro-architectural parameters, Poisson's ratio, and effective elastic modulus, has not been sufficiently addressed. Here, we aim at elucidating the independent effects of the Poisson's ratio on the response of preosteoblast cells within 3D micro-environments.

Advanced micro-additive manufacturing (micro-AM) techniques, such as two-photon polymerization (2PP), have emerged as a valuable tool for exploring the influence of the Poisson's ratio on cell response in 3D micro-/meso–scale structures [41–44]. The 2PP technique creates high-resolution, complex meso–scale structures with micro-metric or sub-micrometric features [45–50], enabling the creation of 3D scaffolds with varying Poisson's ratios and allowing the study of the impact of these properties on the cell behavior in 3D. Moreover, the availability of chemically biocompatible photoresists make the 2PP technique a potential tool in cell biology studies [42].

In this study, we first used computational mechanics and the finite element method (FEM) to rationally design meta-biomaterials with different values of the Poisson's ratio (range of - 0.74 to + 0.74) while maintaining similar values of the effective elastic modulus, porosity, pore size, and strut diameter. Then, we employed the 2PP technique to fabricate these complex meta-biomaterials at the meso–scale (*i.e.,* $1356.0 \times 1356.0 \times 1800.0\ \mu m^3$ with a strut diameter of 36.0 μm) using a methacrylate photosensitive polymer (called IP-Q^{TM}). Subsequently, we measured the mechanical properties of IP-Q at the micro-scale (*i.e.,* a cylinder with equal diameter and height of 30.0 μm) for our FEM models using micro-compression, and similarly, characterized the mechanical properties of the meta-biomaterials at the meso–scale to validate our rational design approach. Finally, we evaluated the response of mouse preosteoblasts seeded onto the meta-biomaterials by assessing their viability, metabolic activity, spatiotemporal organization, as well as osteogenic differentiation and matrix mineralization.

Our study provides new insights into the importance of the Poisson's ratio, as a mechanical cue in the design of meta-biomaterials. This offers new opportunities for developing innova-

tive 3D-engineered micro-environments that can be customized for specific tissue engineering and regenerative medicine applications.

2. Material and methods

2.1. Rational design of the meta-biomaterials

To determine the optimal parameters for the 3D design of meta-biomaterials, we started off with 2D structures to initially guess the mechanical properties. This approach was advantageous as computational modeling of 2D structures is more straightforward than that of 3D structures. Moreover, there is an explicit analytical relationship describing the relationship between the design parameters of hexagonal unit cells and the Poisson's ratio (ν) of the resulting 2D meta-biomaterial [51]:

$$\nu = -\varepsilon_T/\varepsilon_L; \ \nu_{yz} = \frac{\left(\frac{h}{l} + \sin\theta\right)\sin\theta}{\cos^2\theta}, \tag{1}$$

where ε_T and ε_L denote the transverse and longitudinal strains, respectively. The geometrical parameters h, l and θ are illustrated in Fig. 1a.iii. The porosity of such meta-biomaterials is defined as:

$$Porosity = \left(1 - V_{scaffold}/V_{solid}\right) \times 100, \tag{2}$$

where $V_{scaffold}$ and V_{solid} respectively refer to the volumes of the meta-biomaterial calculated from a CAD software and the volume of a solid cube encompassing the entire meta-biomaterial structure ($L_t \times W_t \times W_t$ in Fig. 1a.i).

Furthermore, we defined pore size (*PS*) as the diameter of the largest sphere that can fit within a unit cell of the meta-biomaterials (*i.e.*, the yellow sphere in Fig. 1a.ii).

To rationally design the meta-biomaterials studied here, we employed a combination of a customized Matlab (R2022b) code (Mathworks, US), SolidWorks (2022, Dassault Systèmes, France), and computational models created using a commercial nonlinear FEM code (Abaqus, 2022, Dassault Systèmes, France) for modeling the meta-biomaterials and expediting the process. We applied Eq. (1) to obtain a rough approximation of ν_{yz} and study the effects of geometrical parameters (*e.g.*, h and l, and θ) on it, which is valid for 2D structures. First, we designed a 2D auxetic meta-biomaterial with a large absolute value of the (negative) Poisson's ratio (= −1) to serve as a reference in our mechanical design. Subsequently, we adjusted the geometrical parameters to match the mechanical and morphological properties of the auxetic structure for other designs. Multiple iterations were performed to calculate the longitudinal effective elastic modulus, porosity, pore size, and strut diameter in 2D structures.

Using the initial approximation of these parameters (*e.g.*, unit cells size, pore size and porosity) in 2D and the cell size constraint, we determined the final 3D designs along with their corresponding unit cells (Fig. 1b) via 3D FEM. We assumed the meta-biomaterials are comprised of 6 × 6 × 3 unit cells with an overall dimension of 1356.0 × 1356.0 × 1800.0 μm^3 (in x, z, and y, Fig. 1a.i) with a particular definition of the pore size (Fig. 1a.ii) and parametrized unit cells (Fig. 1a.iii). We first applied two constraints to limit the permitted porosity and pore size. We limited the porosity to the values found for the trabecular bone (*i.e.*, 50–95 %) [52] while the pore sizes were limited to values exceeding 100.0 μm to allow for easy penetration of preosteoblast cells into the meta-biomaterials and to facilitate mass transport. The latter constraint was based on our measurement of the size of the preosteoblast cells (MC3T3-E1) via visualizing their cytoskeleton morphologies, which indicated that the cells were in the approximate range of 50–100 μm (Fig. 1a.iv). The unit cell parameters (*e.g.*, h or l), were, therefore, adjusted to have a similar effective elastic modulus but different Poisson's ratio values. This resulted in a pore size of 180.1 ± 5.3 μm and a strut diameter of 36.0 μm.

It is noted that both effective elastic moduli and Poisson's ratios reported in Fig. 1d and Table 1 were calculated at small strains (= 1%) to minimize the effects of plasticity and damage on the calculation. It is worth noting that to calculate the mechanical and morphological properties of the meta-biomaterials, we used 3D solid elements (instead of beam elements). We merged the struts of meta-biomaterials to create a uniform, single-solid structure. Therefore, no concerns of struts overlapping and multiple mass counting [53] exist.

2.2. FEM analysis

The .step (the standard for the exchange of product data) files of the designs were imported from SolidWorks into Abaqus. To model the constitutive behavior of the base material (IP-Q), which exhibited a highly nonlinear behavior (Fig. 2b.i), we used hyperelastic models, allowing IP-Q to be compressible but assuming it to be isotropic. Different hyperelastic models, including Neo-Hookean ($\Psi = C_{10}(\bar{I}_1 - 3) + \frac{1}{D}(J - 1)^2$), Mooney-Rivlin ($\Psi = C_{10}(\bar{I}_1 - 3) + C_{01}(\bar{I}_2 - 3) + \frac{1}{D}(J - 1)^2$), and third-ordered reduced polynomial ($\Psi = \sum_{i=1}^{3} C_{i0}(\bar{I}_1 - 3)^i + \frac{1}{D_i}(J - 1)^{2i}$) were examined. ψ, $\bar{I}_i$, C_{ij}, D, and j represent strain energy density function, the invariants of the modified Cauchy-Green tensors, distortional response-related coefficients, volumetric response-related coefficients, and total volume ratio, respectively. We calibrated the models based on the uniaxial engineering stress/strain of the polymerized IP-Q under compression loading (Fig. 2b.i), considering strains < 6 %, and calculated the material constants. For this purpose, the engineering stress (**P**, first Piola–Kirchhoff stress tensor) was derived from the strain energy density function as $\mathbf{P} = \partial\Psi/\partial\mathbf{F}$, where **F** is the deformation gradient tensor. In uniaxial compression test, considering λ_x, λ_y and λ_z, as stretches in x, y and z directions, $\mathbf{F}_{3\times3} = [\lambda_x, 0, 0; 0, \lambda_y, 0; 0, 0, \lambda_z]$ with $\lambda_x = \lambda_y$. We found the best curve that fitted on the above-mentioned constitutive models and our experimental data in Matlab (R2022b) (Mathworks, US) to calibrate the material constants. The third-order reduced polynomial model provided the best fit between the modeling and experimental results, ensuring enhanced computational stability with a coefficient of determination (R^2) of 0.9910. The material coefficients for the model were determined as $C_{10} = 52.80$ MPa, $C_{20} = 11521.43$ MPa, $C_{30} = -603444.78$ MPa, $D_1 = 0.0003$ MPa^{-1}, and $D_2 = D_3 = 0$. The very small values of the volumetric response-related coefficients (D_i) indicated that IP-Q is nearly incompressible.

To apply the boundary conditions to the meta-biomaterials, all the degrees of freedom of the reference points (RPs) were kinematically coupled to the corresponding node sets in the model (Fig. 1a.i). RP1, RP2, RP3, and RP4 were respectively located on the top surface of the structures in the xz plane, the left side of the structures in the yz plane, the bottom surface of the structures in the xz plane, and the right side of the structures in the yz plane. In addition, the sets of RP1-RP3 and RP2-RP4 were respectively used to model the meta-biomaterials along the longitudinal and transverse directions. It is worth mentioning that no RP was considered in the xy plane as the meta-biomaterials were transversely isotropic. The nonlinear static solver of Abaqus was used for all the simulations, which were assumed to be quasistatic in nature. Geometric nonlinearities were also considered due to the micro-architectural complexity of the meta-biomaterials. To measure the longitudinal effective elastic modulus (E_L) and Poisson's ratio (ν_{yz} or ν_{yx}), the structures were loaded along the y-direction (loading I) under displacement-controlled conditions. For the transverse effective elastic modulus (E_T), the structures were loaded along the x- or z-direction (loading II) under displacement-
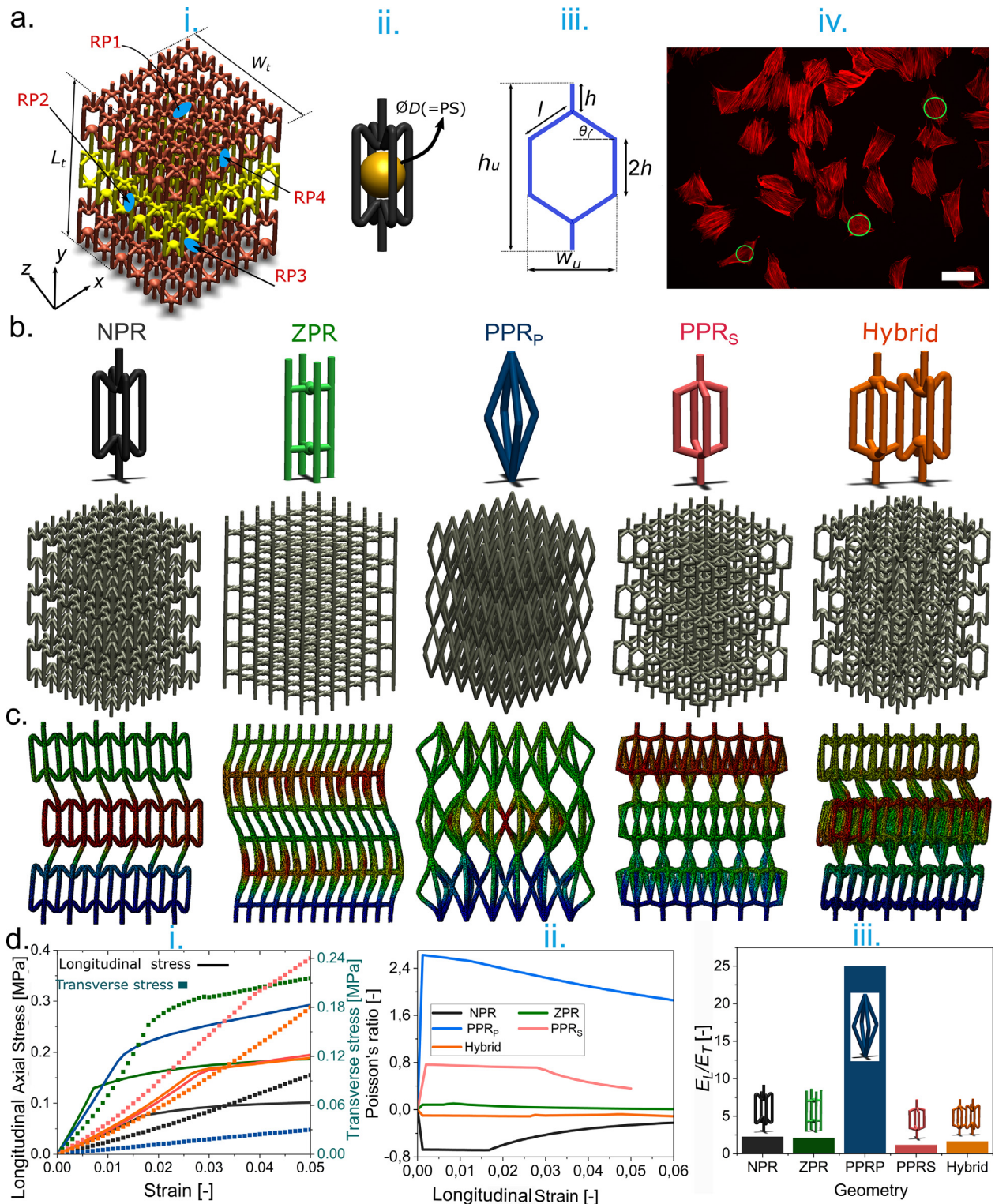
Fig. 1. A schematic illustration of the design process for meta-biomaterials. a.i: A 3D representation of the meta-biomaterials, displaying the corresponding geometrical parameters, a global coordinate system ($x - y - z$), and reference points (*i.e.*, RP1-RP4). L_t and W_t represent the overall height and width of the meta-biomaterials, respectively. a.ii: A depiction of a unit cell of the meta-biomaterials, highlighting the pore size (PS) and the diameter (D) of the yellow sphere. a.iii: A 2D schematic representation of a unit cell of the meta-biomaterials with corresponding geometrical parameters. h_u, w_u, h, l, and θ represent the overall height and width of a unit cell, length of vertical struts, length of tilted struts, and the angle between two struts, respectively. a.iv: The preosteoblast cells after 1 day of culture (immunofluorescence staining of actin). The scale bar represents 100 μm. b. A schematic illustration of the final design of the meta-biomaterials and their corresponding unit cells. c. The deformation pattern of the meta-biomaterials modelled using FEM at 6 % longitudinal strain under quasi-static loading. The contour qualitatively displays the magnitude of the measured displacement in the specified units (blue represents the lowest magnitude while red indicates the highest one). d. The final numerical results of the meta-biomaterials in terms of the longitudinal stresses/strains (i.), Poisson's ratio (*i.e.*, ν_{yz}) (ii.) and the ratio of the longitudinal effective elastic modulus to the transverse one (iii.).

Table 1

Geometrical and mechanical properties of the final design of the meta-biomaterials with their corresponding mean and standard deviations. PS and d_s respectively stand for pore size and strut diameter. Note that the numbers in the table without standard deviations are obtained from computational simulations and CAD designs for which no standard deviations are available.

Type	2D unit cell	Porosity [%]	E_L Exp [MPa]	E_L FEM [MPa]	E_T FEM [MPa]	E_L/E_T [-]	v_{yz} [-]	v_{xz} [-]	v_{xy} [-]	d_s [μm]	PS [μm]
NPR		92.64	9.67 ± 0.40	4.50	2.00	2.25	−0.74	−0.22	−0.22	36.0	184.0
ZPR		92.64	20.00 ± 0.80	18.00	8.60	2.09	0.08	0.05	0.03	36.0	184.0
PPR_p		92.64	16.11 ± 1.10	15.00	0.60	25.00	2.24	−0.59	0.11	36.0	174.7
PPR_s		94.47	10.15 ± 0.40	5.64	5.00	1.13	0.74	−0.22	0.33	36.0	184.0
Hybrid		92.64	13.30 ± 0.60	5.89	3.60	1.64	−0.10	0.00	−0.07	36.0	174.0

controlled conditions. The boundary conditions for the loadings I and II were ($u_{y,RP_3} = 0$, $u_{y,RP_1} = 0.05 \times L_t$) and ($u_{x,RP_2} = 0$, $u_{x,RP_4} = 0.05 \times W_t$), respectively, where u is the displacement. The meta-biomaterials were discretized with 3D quadratic tetrahedral elements of type C3D10. To ensure the robustness of our numerical analyses and achieve mesh-independent results, we performed a mesh sensitivity analysis with varying element sizes. The results of this study demonstrated the values calculated for the effective elastic modulus converge within 4 % when 450,000 elements are used.

The engineering stresses of the simulations were calculated by taking the reaction force derived from the FEM modeling and dividing it by the initial projected cross-sectional area of the meta-biomaterials ($W_t \times W_t$ in loading I and $L_t \times W_t$ in loading II). The engineering strain was calculated by taking the displacement of the relevant RP (RP1 in loading I and RP2 in loading II) and dividing it by the initial height (L_t in loading I) or initial width of the meta-biomaterials (W_t in loading II). Ultimately, the longitudinal and transverse effective elastic moduli were computed using the reaction force of the RPs and the projected cross-sectional areas as:

$$E_L = (F_{RP1}/(W_t \times W_t))/\varepsilon_L; \; E_T = (F_{RP2}/(L_t \times W_t))/\varepsilon_T \quad (3)$$

where F_{RP1}, and F_{RP2}, respectively represent the longitudinal reaction force of RP1 (in loading I), and the longitudinal reaction force of RP2 (in loading II).

The Poisson's ratios in two orthogonal planes (*i.e.*, $v_{yz} (= v_{yx})$, $v_{xy} (= v_{zy})$, and $v_{xz} (= v_{zx})$) were calculated using the following equations:

$$v_{yz} = -(\bar{u}_{z-right} - \bar{u}_{z-left})/(W_t \times \varepsilon_{y,L}) : \text{loading in the } y-\text{direction}$$

$$v_{xy} = -(\bar{u}_{y-bottom} - \bar{u}_{y-top})/(L_t \times \varepsilon_{x,L}) : \text{loading in the } x-\text{direction}$$

$$v_{xz} = -(\bar{u}_{z-right} - \bar{u}_{z-left})/(W_t \times \varepsilon_{x,L}) : \text{loading in the } x-\text{direction} \quad (4)$$

where $\bar{u}$ indicates the average displacements of the nodes on the corresponding surfaces. For example, $\bar{u}_{z-right}$ shows the average displacement of the nodes in the z-direction that are placed on the right side of the meta-biomaterial in Fig. 1a.i. Also, $\varepsilon_{x,L}$ and

$\varepsilon_{y,L}$ correspond to the applied longitudinal strains in the x- and y-directions, respectively.
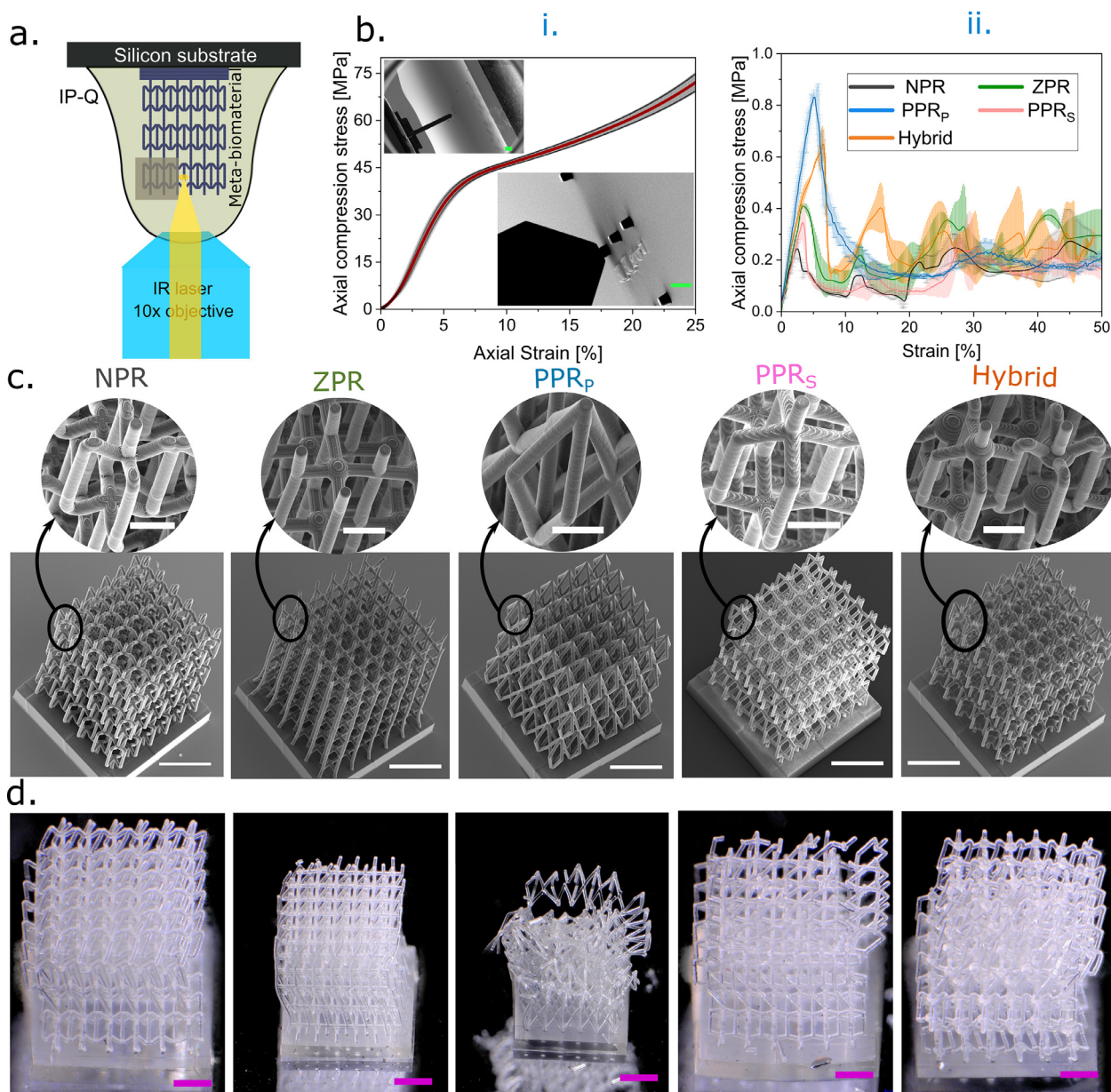
2.3. 2PP-based fabrication of the meta-biomaterial specimens

The meta-biomaterials were fabricated using 2PP. Their designs were created using a commercial computer-aided design (CAD) software, SolidWorks (Dassault Systèmes, France), and exported as a .stl (standard triangle language) file. These .stl files were then imported into the DeScribe software (Nanoscribe, Germany) to generate General Writing Language (.gwl) files. The .gwl files were subsequently imported into Nanowrite (printing software, Nanoscribe, Germany) for connection to the 2PP 3D printer, facilitating the fabrication of the final meta- biomaterials. The specimens were then printed using a Photonic Professional GT+ (Nanoscribe, Germany) 3D printer.

The dip-in laser lithography (DiLL) configuration was employed, with a 10× objective featuring a numerical aperture (N.A) of 0.30. The lens was chosen based on the size of the specimens and solid/void features that needed to be reproduced. A negative tone-methacrylate-based photoresist known as IP-Q (Nanoscribe, Germany) with a refractive index of 1.49 was used as photoresist. The specimens were printed on silicon substrates ($25 \times 25 \times 0.7$ mm³ in dimensions, Nanoscribe, Germany) featuring a refractive index of 3.71.

Furthermore, as the 3D meta-biomaterials exceeded the writing field and working distance of the 10× objective (707.10×707.10 μm² and 700 μm, respectively), we divided them into smaller blocks (Fig. 2a). We also conducted multiple printing trials to refine the printing parameters, particularly for the NPR and Hybrid groups. These two groups theoretically had some features that need supports, which were practically challenging to print. To overcome this challenge, we employed a piezo scanning mode instead of z-drive for the stage movement. This approach was chosen because z-drive movement can cause mechanical stage movement and photoresists instability, potentially leading to micro-movement and print imperfection. Another technique to avoid photoresist instability immediately after the print starts is to decelerate the mechanical movement of the stage for printing blocks that likely require support. This was achieved by reducing the acceleration and velocity of the stage to 5 mm s^{-2} and 100 mm s^{-1}, respectively.

Fig. 2. a. A schematic representation of the 2PP technique employed for fabricating meta-biomaterials from IP-Q photoresist on a silicon substrate using a laser (10× objective). b. The mechanical evaluation of IP-Q cylinders (i) and meta-biomaterials (ii); i. The engineering stress-strain curves measured for IP-Q-based specimens at the micro-scale under 25 % strain and a strain rate of 0.25 μm s⁻¹. The scale bars in the upper and lower images correspond to 50 and 500 μm, respectively. The red and black lines represent mean and standard deviation, respectively. ii. The compression testing of the meta-biomaterials at 50 % strain (1 mm displacement) performed with a displacement rate of 10 μm s⁻¹. c. The SEM images of meta-biomaterials 3D printed using 2PP, showcasing their respective unit cells at higher magnifications. The scale bars for the overall structures and unit cells measure 500 and 100 μm, respectively. d. The optical microscopy of compressed meta-biomaterials at 50 % strain (1 mm displacement) when tested using a displacement rate of 10 μm s⁻¹. The scale bar represents 300 μm.

To improve print quality in solid structures, we considered the integration of a block shear angle (the angle between the stitched designs) with a specific overlap. Since the meta-biomaterials consisted of tilted struts, it is important to consider the effects of the tilted struts' angles (*i.e.*, θ) and block shear angle at the same time. A proper block shear angle is recommended so that the stitching planes create an angle between the material and themselves. In this case, a block shear angle close to zero is favorable for NPR, PPR_p, PPR_s, and Hybrid groups, as these structures had already tilted struts. For the ZPR group, however, a block shear angle of 20° was chosen, as there are no tilted struts.

Additionally, overlaps between the segments and the number of contours as well as their distances were adjusted to optimize

the print quality of the NPR and Hybrid groups. This was accomplished by conducting several tests on a unit cell of the NPR group (without stitching) to determine the optimal conditions for these parameters.

Before printing the meta-biomaterials, the silicon substrates were cleaned with acetone and isopropyl alcohol (IPA; both from Sigma-Aldrich, Germany) using a lint-free wipe and were subsequently blow dried with nitrogen. To further clean and activate the surface of the substrates, an oxygen plasma cleaner (Diener electronic GmbH, Germany) was employed at 80 W with a gas flow rate of 5 cm³ min⁻¹, and a pressure of 0.12 bar for 15 min. To enhance the adhesion between the specimens and substrates, silanization with 3–(Trimethoxysilyl) propyl methacrylate (Sigma-

Aldrich, Germany) was performed for 1 hour. Silanization facilitates effective chemical bonding by rendering the substrate surface hydrophobic. A suitable concentration of 3-(Trimethoxysilyl) propyl methacrylate was established at 2.67 % v/v by diluting it with ethanol. Following silanization, the specimens were washed with acetone, distilled water, and were then air-dried.

After exposing the specimens, the samples were immersed in propylene glycol methyl ether acetate (PGMEA, Sigma-Aldrich, Germany) for 1 hour in a borosilicate Petri dish to dissolve the unpolymerized photoresist. Subsequently, the specimens were rinsed with IPA for 5 min in a Petri dish to remove the PGMEA. To further reduce capillary force-induced deformation in the structures and to provide stronger bonding between the specimens and silicon substrates, Novec 7100 engineered fluid (Sigma-Aldrich, Germany) was applied for 30 s, as this solvent exhibits a lower surface tension than IPA.

2.4. Micro-mechanical test experiment

To measure the mechanical properties of the polymerized IP-Q at the micro-scale and integrate them into our FEM models, a compression test was performed on standard micro-cylindrical specimens with equal diameter and height of 30.0 μm using the FT-NMT03 nano-mechanical testing system (FemtoTools, FT-NMT03, Switzerland). The specimens were 3D printed using 2PP with the same parameters as the actual meta-biomaterials, which included a laser power of 50 mW, a scanning speed of 100,000 μm/s, a slicing distance of 5 μm, and a hatching distance of 1 μm. We assumed that the IP-Q possessed isotropic elastic properties. A 200,000 μN silicon probe with a tip cross-section of 50×50 μm^2 was employed to compress the specimens. To visualize the interface between the probe and the specimens, the FT-NMT03 machine was integrated into a scanning electron microscope (JSM-6010LA, LEOL, Japan). To account for the stiffness of the silicon substrate and the adhesive used between the substrate and sample holder, the substrate's stiffness was initially measured at a 0.25 μm s^{-1} displacement rate with a 3 μm displacement. Following this, the compression experiment was conducted at the same displacement rate but at a 25 % strain, after establishing contact between the probe and specimen. The final engineering (nominal) stress and strain were obtained by dividing the derived force and loading displacement to the initial cross-section area and initial length, respectively.

2.5. Macro-mechanical compression test

To measure the mechanical properties of the meta-biomaterials at the macro-scale, a mechanical uniaxial test machine (LLOYD instrument LR5K, UK) with a 5 N load cell was employed. All the experiments were conducted in the compression mode at a stroke rate of 10 μm s^{-1} until 50 % strain. The acquired force-displacement data was used to calculate the engineering stress and engineering strain of the specimens by dividing them by the initial projected cross-section and by the height of the specimens, respectively. The effective elastic modulus of the meta-biomaterials was then determined from the linear portion of the engineering stress-strain curve.

2.6. Preosteoblast cell culture

Mouse preosteoblast cells (MC3T3-E1, Sigma Aldrich, Germany) were pre-cultured in alpha minimum essential medium (α-MEM without nucleoside) supplemented with 10 % (v/v) fetal bovine serum and 1 % (v/v) penicillin-streptomycin (all from Thermo Fisher Scientific, US) for one week at 37 °C and 5 % CO$_2$. The culture medium was refreshed every 2 days. To sterilize the specimens, they were first immersed in 70 % ethanol for 10 min, fol-

lowed by twice submersion in 1× PBS (Sigma Aldrich, Germany). Subsequently, the specimens were exposed to UV light for 20 min. For all biological assessments except for the PrestoBlue assay, the specimens were glued to a transparent PMMA substrate (9 mm in diameter and 2 mm in thickness) using a biocompatible silicone adhesive and were placed in a 24-well plate. The cells were seeded on the specimens along the y-direction (1×10^5 cells per sample) in a 24-well plate. After 4 h of incubation, the specimens were transferred to new well plates (Greiner, Bio-One, The Netherlands). From day 2, the cells were supplied with osteogenic medium containing 50 μg mL^{-1} ascorbic acid (1:1000) and 4 mM β-glycerophosphate (1:500) (both from Sigma Aldrich, Germany). All the cell culture experiments were conducted with at least three replicates per group, and two independent experiments were carried out for each assay.

2.7. Immunofluorescence staining of the cytoskeleton

The cells were fixated by washing the specimens with 1× PBS twice, followed by immersion in 4 % (v/v) formaldehyde solution (Sigma Aldrich, Germany) for 10 min. After washing the cells with 1× PBS twice, they were permeabilized by immersion in 0.5 % Triton X-100/PBS solution (Sigma Aldrich, Germany) at 4 °C for 5 min, followed by incubation in 1 % BSA/PBS (Sigma Aldrich, Germany) at 37 °C for 5 min. Anti-vinculin mouse monoclonal primary antibody (1:100 in 1 % BSA/PBS, Sigma Aldrich, Germany) and rhodamine-conjugated phalloidin (1:1000 in 1 % BSA/PBS, Thermo Fisher Scientific, US) as a primary antibody were added followed by incubation for 1 hour at 37 °C. This was followed by washing the cells in 0.5 % Tween-20/PBS (Sigma Aldrich, Germany) three times for 5 min each. The specimens were then incubated again in Alexa Fluor 488, donkey antimouse polyclonal secondary antibody (1:200 in 1 % BSA/PBS, Thermo Fisher Scientific, US) at room temperature for 1 h. Finally, the specimens were washed with 0.5 % Tween-20/PBS three times for 5 min each, followed by 5 min washing with 1× PBS.

2.8. PrestoBlue assay

This assay was used to measure the metabolic activity of the cell-laden meta-biomaterials after 1, 3, 6, 8, 10, 13, and 17 days of culture. Accordingly, the specimens ($n = 4$) were placed in a 96-well plate without the PMMA substrates (with 300 μL of α-MEM). α-MEM with 10 % PrestoBlue (300 μL, Thermo Fisher Scientific, US) was added and the specimens were incubated for one hour at 37 °C and 5 % CO$_2$. Subsequently, 100 μL of the incubated medium was transferred to a 96-well plate (Greiner, Bio-One, The Netherlands) in duplicate. Finally, the metabolic activity of the specimens was measured by using a Victor X3 micro-plate reader (PerkinElmer, Groningen, The Netherlands) at a 530 nm excitation wavelength and 595 nm emission wavelength.

2.9. SEM imaging

To conduct SEM imaging, the specimens were washed and fixated following the same steps as for cytoskeleton staining. After washing the specimens with 1× PBS, followed by distilled water for 5 min (twice each step), the specimens were dehydrated in 50 %, 70 %, and 96 % ethanol for 15, 20, and 20 min, respectively. Subsequently, the specimens were dried in air overnight at room temperature. Prior to SEM imaging, gold sputtering was performed on all the specimens at 20 mA for 20 s twice in ±45° tilted configurations to ensure a homogeneous distribution of the gold layer with a thickness of ∼12 nm. An SEM (JEOL JSM-IT100, Japan) was used to image the specimens.

2.10. Runx2 staining

First, the specimens were fixated and permeabilized following a similar procedure as for F-actin. The specimens were then incubated in a dilution of primary and secondary antibodies, including Runx2 rabbit monoclonal primary antibody (1:250 in 1 % BSA/PBS, Abcam, UK), and Alexa Fluor 488, donkey anti-rabbit polyclonal secondary antibody (1:200 in 1 % BSA/PBS, Thermo Fisher Scientific, US), respectively.

2.11. Alizarin red staining (ARS)

Initially, the specimens were fixated using the same fixation procedure. The specimens were then incubated in 2 % (w/v) ARS solution (Sigma Aldrich, Germany) for 30 min in the dark, followed by washing them five times with distilled water.

2.12. Fluorescence microscopy

A fluorescent microscope (ZOE fluorescent cell imager, Bio-Rad, The Netherlands) was employed to visualize the cytoskeleton of the stained cells (20× objective featuring 0.4 NA).

2.13. Live/dead assay

After washing the meta-biomaterials with $1\times$ PBS twice, a solution of 2 μM calcein and 3 μM ethidium homodimer-1 (both from Thermo Fisher Scientific, Waltham, MA, USA) in 1 ml $1\times$ PBS was added to the specimens, which were then stored in dark for 30 min at room temperature.

2.14. Confocal imaging

A confocal microscope (Zeiss LSM 710, USA) with a 10× objective and 0.25 NA (air configuration) was used to image the Runx2 and ARS. The confocal microscope covered 263 μm (25 slices of z-stack). A laser with 50 % power (max power of 0.35 mW) at a wavelength of 543 nm was used. For ARS, only one channel with excitation and emission wavelengths of 543 and 562 nm, respectively, was used. For Runx2, a laser with a wavelength of 488 nm and 60 % power (max power of 5.93 mW) with two channels (488 nm and 540 nm) and (543 nm and 562 nm) was employed for the excitation and emission wavelengths, respectively.

2.15. Image analysis

To quantitatively compare the expression levels of Runx2 and ARS, Fiji (ImageJ, National Institutes of Health, USA) was utilized. The .czi images from the confocal were imported into fiji prior to the measurement. To measure the maximum intensity and modification of the images, a macro code (.ijm) was written. The contrast of all the images were enhanced by 0.35 saturated pixels and the final images were derived based on the maximum intensity of each layer.

2.16. Statistical analysis

Origin (2022, USA) was used for the micro- and macro-mechanical tests for the calculation of the means and standard deviations. Prism (9.4.1, GraphPad, US) was also utilized for biological results, including metabolic activity, shrinkage of the meta-biomaterials, and osteogenic responses (*i.e.*, Runx2 and ARS) to calculate the mean and standard deviations, adjusted *p*-value, and effect size (*i.e.*, eta-squared (η^2) and Cohen's *d* values). All the experiments were performed with at least three replicates, and two independent sets of biological experiments for the statistical analyses. We performed a normality test using the Shapiro–Wilk test with alpha= 0.05, to confirm the normal distribution of the data in each group. Moreover, the repeatability of the second independent set of the biological experiments were assessed via the Student's T-test. We also performed ordinary one-way ANOVA test, followed by post-hoc analysis using the Tukey's multiple comparison test for considering the interaction effect between groups. It is noted that for all the experiments and graphs, a $p - value < 0.05$ was considered as statistically significant. Moreover, η^2 was calculated based on the ratio of the sum of squares between groups and the total sum of squares [54]. For pairwise analysis, the Cohen's *d* value was calculated based on the ratio of the mean differences between two groups and the total pooled standard deviation of the same two groups as follows [55]:

$$Cohens'd \text{ value} = \frac{(M_1 - M_2)}{SD_{pooled}}; \ SD_{pooled}$$

$$= \sqrt{\frac{(n_1 - 1) \times SD_1^2 + (n_2 - 1) \times SD_2^2}{n_1 + n_2 - 2}} \qquad (5)$$

where *M*, *SD*, n, and SD_{pooled} indicate the mean of each group, the standard deviation of each group, the sample size of each group, and the pooled standard deviation of two groups 1 and 2, respectively. The subscripts 1 and 2 represent groups 1 and 2, respectively. Moreover, *F* (*DFn*, *DFd*) ratio shows the distribution of degrees of freedom in the numerator (*DFn*) and the dominator (*DFd*), and was defined as the ratio of the mean square between groups and within groups. We reported the η^2 and *F* (*DFn*, *DFd*) values for the comparison groups in which a statistically significant difference at each timepoint was observed.

3. Results

3.1. Design of the meta-biomaterials

Five distinct structures with controlled Poisson's ratios, namely negative (NPR), zero (ZPR and Hybrid), and positive (PPR$_p$ and PPR$_s$), were designed based on the results of the computational models (Fig. 1b-d). The NPR, PPR$_s$ and Hybrid (a combination of NPR and PPR) designs were created with the same porosity, longitudinal effective elastic modulus (= E_L, Fig. 1d.i), pore size, strut diameter, and overall dimensions. The PPR$_p$ exhibited almost identical porosities but different values of the effective longitudinal elastic modulus as compared to the NPR meta-biomaterial. The ZPR meta-biomaterial featured a near-zero Poisson's ratio (Fig. 1d.iii), but a different pore shape as compared to the Hybrid one. The designed structures exhibited different mechanical behaviors when loaded in different directions (*x* or *y*), as they were transversely isotropic structures. We, therefore, reported the transverse effective elastic modulus (= E_T, Fig. 1d.i) and its ratio to the longitudinal effective elastic modulus (Fig. 1d.iii and Table 1).

We also assessed the deformation pattern of the meta-biomaterials under a certain compression strain (= 6 %) (Fig. 1c). The designs with negative and zero Poisson's ratio exhibited different modes of deformation (lateral sliding), unlike those with positive values of the Poisson's ratio (*i.e.*, ν_{yz}). The mechanical and morphological parameters of the final design of the meta-biomaterials are presented in Table 1. It is worth mentioning that the PPR designs (*i.e.*, PPR$_p$ and PPR$_s$) exhibited negative Poisson's ratio in one direction (*i.e.*, ν_{xz}, Table 1). We believe that this can be improved in further studies by considering three symmetric planes in the design of the meta-biomaterials.

3.2. 3D printing and mechanical characterization of the meta-biomaterials

We used 2PP to fabricate the designed meta-biomaterials at the micro-scale (Video 1 of the supplementary document and Fig. 2a). However, printing complex micro-structures via 2PP requires finding refined printing parameters (*e.g.,* laser power, scanning speed, slicing distance (the *z*-distance between two adjacent layers), and hatching distance (the *x*-, and *y*- distance between two adjacent polymerized lines)), stitching parameters (*e.g.,* block size, block shear angle and connection between blocks), scanning mode (piezo or *z*-drive), and acceleration and movement of the stage. Structures that needed to be supported during the printing process, such as NPR and Hybrid, required careful attention to ensure high-quality prints. The detailed printing parameters are described in the experimental section.

We measured the mechanical properties of IP-Q at the micro-scale and found that its engineering stress-strain curves are highly nonlinear (Fig. 2b.i and Video 2 of the supplementary document). We considered such nonlinearity (hyperelastic behavior) in the modeling of the meta-biomaterials through the third-order reduced polynomial hyperelastic model. Based on the material's behavior at the small scale, the Young's modulus of the IP-Q was found to be 823.00±23.12 MPa (mean value ± SD).

To characterize the macro-mechanical properties of the 3D printed specimens (Fig. 2c), we obtained the engineering stress-strain variation (Fig. 2b.ii). The stress values, represented by the mean values with their corresponding standard deviations as shaded regions, display significant fluctuations, which can be attributed to the densification and possible damage (at higher strains) in the studied lattice structures. We focused on the initial linear part of the stress/strain graph (*i.e.,* < 2 % axial strain) to determine the effective elastic modulus of our specimens (Fig. 2b.ii, and Table 1).

It is worth noting that we included a solid pedestal (1400×1400×200 μm^3) beneath each scaffold (Fig. 2c). The addition of the solid pedestal was required to prevent the specimens from moving and ensure their stability during cell culture, thus facilitating subsequent handling and processing steps. This modification is expected to be particularly helpful in the development of complex and delicate biofabricated structures with low relative densities (< 10 %), where maintaining their stability and avoiding potential disruptions during cell culture is of utmost importance.

The deformation patterns of meta-biomaterials following compression tests were captured using an optical microscope (Fig. 2d). In these tests, the structures, particularly in the middle part, were observed to deform laterally, either to the right or left, under large deformation at 50 % longitudinal strain.

3.3. Adhesion and growth of the preosteoblast cells

The polymerized IP-Q resin employed for the creation of the meta-biomaterials was found to be cytocompatible, following viability tests conducted on the MC3T3-E1 preosteoblasts (Figure S1 of the supplementary document). The cells were able to adhere, grow, and migrate upwards to the top surfaces of the structures in about 6 days, as confirmed by SEM imaging after various culturing times (Fig. 3). This was supported by the seeding along the *y*-direction (Fig. 1a.i), which facilitated cell growth through the pores and onto the flat pedestal. The micro-architectures of the unit cells promoted the upward growth of the cells. After 17 days, the cells had already covered the entire meta-biomaterials. However, it was observed that the NPR scaffolds had fewer cells as compared to the other structures (Figs. 3, 4; days 6 and 10).

Interestingly, increasing the cell culture time revealed local bending of the struts in the cell-laden meta-biomaterials (Figs. 3, 4,

and S2 of the supplementary information). As cells grew upward, they appeared to crawl along the struts, stretching them until the entire meta-biomaterial was covered. This resulted in local bending, which was more pronounced in the NPR group than in the other groups.

Cell growth together with the shrinkage of the cells as well as the meta-biomaterials over time induce 3D deformation in meta-biomaterials (see Figs. 3 and 4b, with statistical data reported in Table S1 in the supplementary information). This effect was particularly prominent in the PPR$_p$ group, where the shape of the structure transitioned from a cuboid to a pyramid.

To determine whether the observed substantial deformation is a result of living cells interacting with the meta-biomaterials, a control group without cells on day 17 was also examined. This group underwent the same culture, fixation, and dehydration conditions as the cell culture specimens with cells (first column of Fig. 3). To quantify the deformation of these meta-biomaterials, the shrinkage of their top surface was measured (Table 2). It should be noted that the shrinkage was calculated based on a comparison between the initial configuration immediately after fabrication and the current surface area.

The induced deformation in the cell-free meta-biomaterials was negligible for the NPR, ZPR, PPR$_s$ and Hybrid groups on day 10, except for the PPR$_p$ group. The PPR$_p$ group exhibited an average shrinkage of 29.1 % on day 17, which warrants consideration when evaluating the final deformation attributed to the cells (Fig. 3, first column).

Furthermore, to ascertain whether the deformation observed in the meta-biomaterials was attributable to living cells interacting with the structures or cell shrinkage during SEM imaging processes, we quantified the shrinkage of the meta-biomaterials before fixation and dehydration on day 17 (Fig. 3, last column, control with cells before fixation and dehydration). The optical images of the meta-biomaterials (top surfaces) revealed that PPR$_p$ group had experienced the highest degree of shrinkage as compared to the other meta-biomaterials (46.1% *vs.* 21.1 %). This finding suggests that the final deformation depicted in the SEM images resulted from both the forces exerted by the cells and the shrinkage caused by cell dehydration and specimen processing.

3.4. Metabolic activity and osteogenic response of the preosteoblast cells

The metabolic activity of the cells seeded on the different meta-biomaterials increased with time (Fig. 4c, with statistical data reported in Table S2 in the supplementary information), indicating that the cells could proliferate and grow within the micro-porous structures. It is important to note that, to account for the effects of the metabolic activity of the initial cell population, the metabolic activities were normalized by dividing them by their corresponding day 1 value. This adjustment was made because most cells were situated on the pedestal during the early stages of cell culture (Figs. 3 and 4). The PPR$_p$ and PPR$_s$ groups displayed the highest metabolic activity at later time points, while the NPR group had the lowest (Fig. 4c).

To evaluate the osteogenic response of the preosteoblast cells, three groups were selected, namely NPR, PPR$_p$, and Hybrid. The NPR group comprised meta-biomaterials with an extremely negative value of the Poisson's ratio, the PPR$_p$ represented meta-biomaterials with an extremely positive value of the Poisson's ratio (*i.e.,* ν_{yz}) as a counterpoint to the NPR group, and the Hybrid group served as a control group possessing almost the same effective elastic moduli and porosity as the NPR group but with a near-zero Poisson's ratio. The osteogenic differentiation of the cells was assessed by measuring the expression of Runx2 after 10 days of culture (Fig. 5a.i and b.i and Video 3–8 of the supplementary
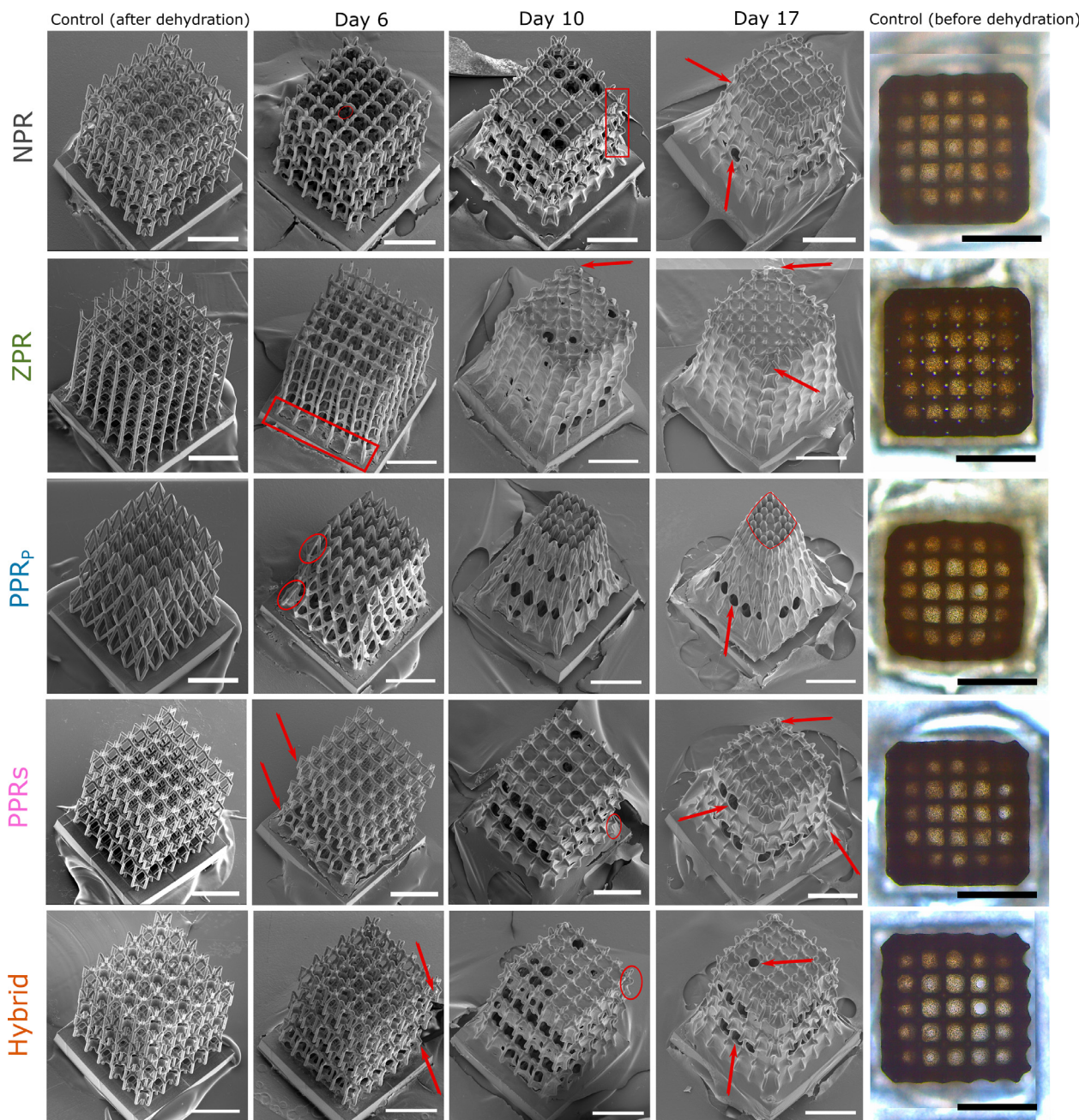
Fig. 3. SEM images of cell-laden meta-biomaterials on various days of the cell culture experiments. Included are optical microscopy images of control specimens without cells post-fixation and dehydration (day 17, first column), and control specimens with cells pre-fixation and dehydration after a 17-day culture period. Scale bars for all the SEM and optical microscopy images measure 500 and 700 μm, respectively. Red annotations highlight local deformations resulting from cellular growth.

Table 2
The shrinkage ratio of the top surface of the cell-free meta-biomaterials (after dehydration) and cell-laden meta-biomaterials (before dehydration).

Type	NPR [%]	ZPR [%]	PPR$_p$ [%]	PPR$_s$ [%]	Hybrid [%]
Control (no cell after dehydration), day 17	5.9 ± 0.5	9.3 ± 1.1	29.1 ± 2.1	7.0 ± 0.6	12.7 ± 0.9
Control (with cells before dehydration), day 17	21.1 ± 1.0	24.1 ± 2.4	46.1 ± 3.1	22.2 ± 2.0	21.6 ± 1.1

document) whereas matrix mineralization was assessed by Alizarin red staining of the matrix after 17 days of culture (Fig. 5a.ii and b.ii and Video 9–14 of the supplementary document). Both assessments were representative of the top surface of the scaffolds and not the entire 3D structures.

After 17 days of culture, a mineralized matrix was detected in all the three different meta-biomaterials (Fig. 5a.ii and b.ii). Interestingly, the mineralized matrix presents on the surface of the NPR specimens, which exhibited less cell coverage, featured a relatively ordered pattern (predominantly within the pores).
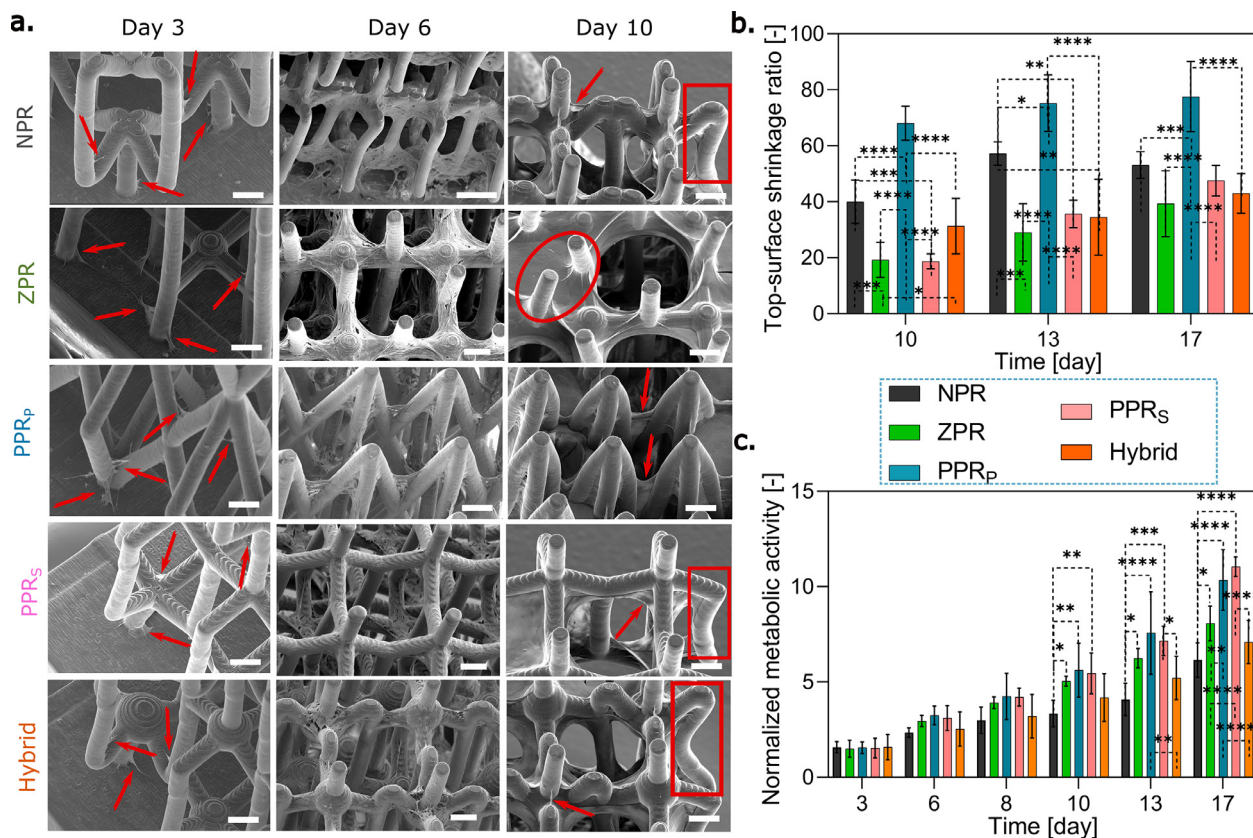
Fig. 4. a. High-magnification SEM images of meta-biomaterials exhibiting local deformation (bending) induced by cellular activity. Red arrows indicate cell presence, while ellipses and rectangles highlight cell-induced deformation (bending). The scale bar measures 50 μm, except for the NPR image at day 6, which has a 100 μm scale bar. A quantitative analysis of the SEM-measured deformations, represented as the shrinkage ratio of the top-surface of the meta-biomaterial specimens, with (p – value = $<$ 0.0001, $F_{(4, 23)} = 48.19$, $\eta^2 = 0.8934$), (p – value = $<$ 0.0001, $F_{(4, 25)} = 26.09$, $\eta^2 = 0.8068$) and (p – value = $<$ 0.0001, $F_{(4, 25)} = 17.30$, $\eta^2 = 0.7346$) on days 10, 13 and 17, respectively. c. The normalized metabolic activity of the cells across a 17-day culture period (relative to day 1), with (p – value, F ($DFn = 4$, $DFd = 32$), η^2) of (0.0009, 6.150, 0.4346), ($<$ 0.0001, 10.07, 0.5573) and ($<$ 0.0001, 29.15, 0.7846) on days 10, 13 and 17, respectively. Statistical significance is denoted by *, **, ***, **** corresponding to p – value $<$ 0.05, p – value $<$ 0.01, p – value $<$ 0.001, and p – value $<$ 0.0001, respectively. The non-asterisks groups indicate that the differences between the groups are not statistically significant (*i.e.*, p – value $>$ 0.05).

4. Discussion

4.1. Rational design and fabrication of the meta-biomaterials

The developed meta-biomaterials with controlled Poisson's ratio were found to influence the response of preosteoblast cells. To design the meta-biomaterials studied here, several physical parameters, including, porosity, pore size, strut diameter, and effective elastic modulus (∼stiffness), were considered to mimic the properties of trabecular bone as much as possible. Nevertheless, the effective elastic modulus of the developed meta-biomaterials was not still in the range of the trabecular bone (0.04–1 GPa [6,8]). This point can be addressed either by adjusting the micro-architecture of the meta-biomaterials or by changing the base material from which the meta-biomaterials are made. Geometry-based adjustment of the effective elastic modulus of the meta-materials can be achieved by changing the strut diameter, changing the angle between the struts (θ), and modifying the ratio of the height of the unit cells to their width (*i.e.*, h_u/w_u in Fig. 1a.iii). As such, increasing strut diameter leads to increased values of the effective elastic modulus while also drastically decreasing the Poisson's ratio. Changing the angle between the struts (θ) can disrupt the compatibility between the pore sizes of the designs and affect the effective elastic modulus. The h_u/w_u value affects the pore size, effective elastic modulus, and porosity such that a lower ratio leads to better consistency for pore size, considering the cell size and the similarity of pore sizes in both PPR and NPR meta-biomaterials.

Another approach for manipulating the effective elastic modulus of meta-biomaterials is to modify the additive manufacturing parameters. For example, the Young's modulus of the base material (IP-Q) varies during the 2PP process as the delivered dose of energy (*i.e.*, laser power × scanning speed^{-1}) increases [56], or as the slicing distance and hatching distance [56] decrease. Modifying some other printing parameters (*e.g.*, by switching between alternate and non-alternate hatch lines) may also have similar effects. However, decreasing the scanning speed, slicing distance, or hatching distance drastically increases the printing time for such complex meta-biomaterials. We optimized the final designs and printing parameters considering the complexity of the designs, printing quality, printing time, while also decoupling their Poisson's ratio from other properties. More details of the optimization process used to adjust the parameters of the manufacturing process can be found in the experimental section.

The meta-biomaterials in this study exhibited transversely isotropic behavior, meaning that they had two planes of symmetry. This resulted in two effective elastic moduli (*i.e.*, E_{xx}, and E_{yy}) and three Poisson's ratios (*i.e.*, ν_{yz}, ν_{xz}, and ν_{xy}). In the longitudinal direction (*i.e.*, y-direction), the Poisson's ratio was decoupled from other mechanical and morphological parameters in some designs, particularly, the NPR and PPRs. However, it is yet not decoupled from effective elastic modulus in the transverse direction (*i.e.*, E_{yy}), Table 1. One way to overcome this is to design a fully isotropic meta-biomaterials with three symmetrical planes (*i.e.*, xy, zy, and xz). In this case, only one effective elastic modulus and one Pois-
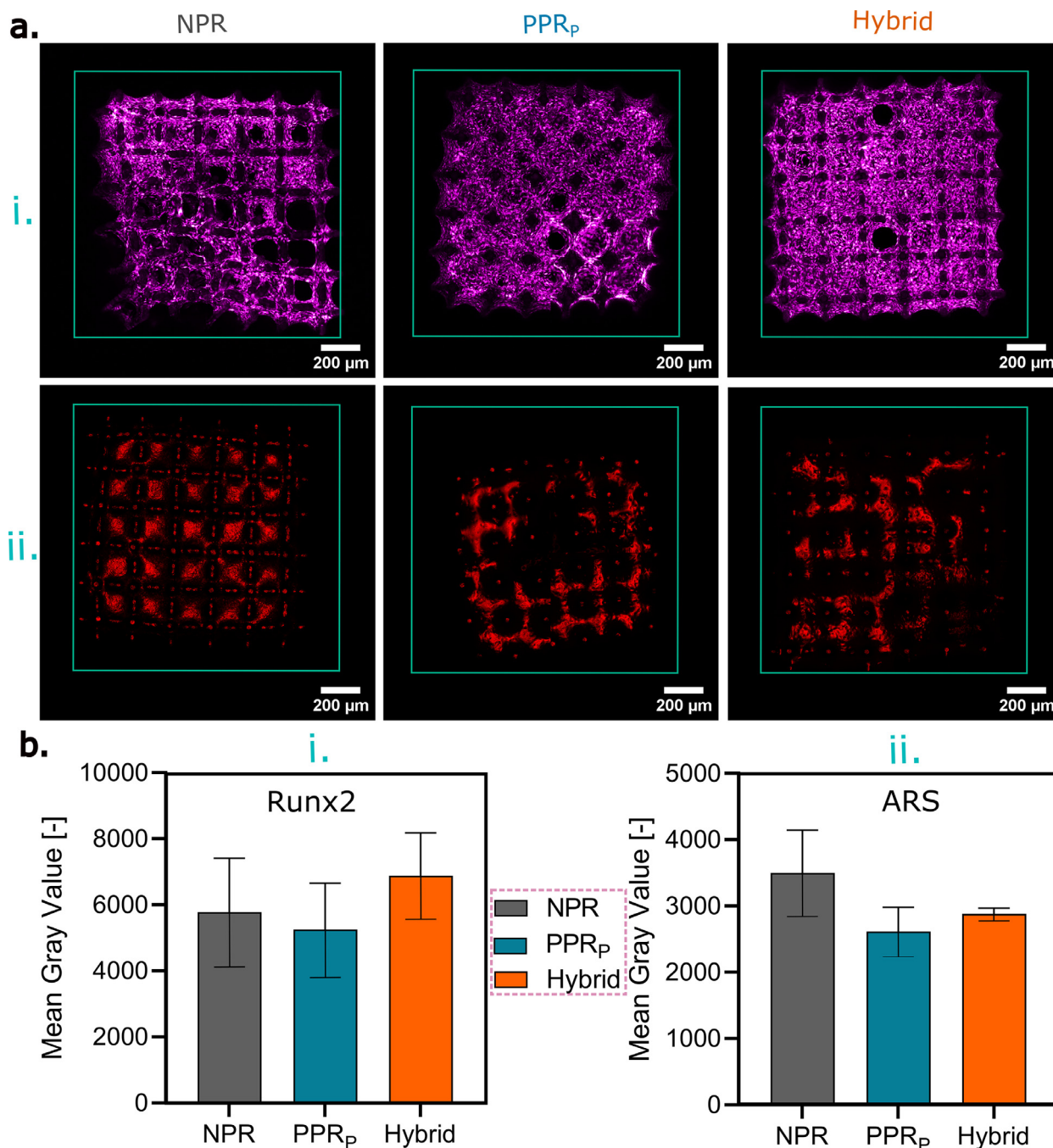
Fig. 5. The osteogenic responses of preosteoblasts-laden meta-biomaterials. **a.** The confocal microscopy images of Runx2 (**a.i**) and mineralized matrix (**a.ii**) on days 10 and 17, respectively. The green rectangle represents the initial cross-section of the meta-biomaterials post-fabrication. **b.** A quantitative analysis of Runx2 (**b.i**) and mineralized matrix (**b.ii**). No statistically significant differences were detected ($p > 0.05$) for the Runx2 and ARS assays.

son's ratio would be enough to characterize the meta-biomaterials, and therefore, the decoupling procedure may become less challenging.

We used 2PP and IP-Q photoresist for fabricating the meta-biomaterials studied here because our primary objective in the current study was to understand the response of bone cells (*e.g.,* cell growth and differentiation) to meta-biomaterials with micro-architectural dimensions that are of the same order of magnitude as the size of individual cells. While it is important to study the effects of the fabrication technique and the constituting material on the response of cells to such meta-biomaterials, the options for such types of studies are currently limited be-

cause 2PP is the only 3D printing technique capable of generating free-form architected biomaterials with such small dimensions and with precisely controlled architectures. Moreover, changing the fabrication technique can influence the surface properties of the produced meta-biomaterials, which might subsequently affect cell responses. All these potential effects need to be studied in the future.

While the overall quality of the printed meta-biomaterials was assessed using SEM, the quality of the 3D printed meta-biomaterials can be further analyzed in future via other imaging techniques, such as micro-computed tomography (μ-CT) or confocal microscopy.

4.2. Mechanical characterization

The experimental and numerical values of the longitudinal effective elastic modulus were in good agreement (Table 1, ZPR and PPR$_p$ groups). We attribute the slight discrepancies between the experimental and numerical values to errors in the micromechanical compression tests, the inaccuracies of the macromechanical uniaxial test machine, the print quality, and the post-development shrinkage of the structures.

Regarding the pattern transformation of the meta-biomaterials under compression test, the specimens with positive Poisson's ratios were unable to withstand such large deformations while those with zero or negative Poisson's ratios deformed without failure up to 50 % longitudinal strain. This was attributed to the much larger E_L/E_T value of the PPR$_p$ group as compared to the other experimental groups. The NPR, PPR$_s$, and Hybrid specimens had the same values of the effective elastic modulus but highly different ultimate strengths (Fig. 2a.ii). For the structures with the same effective elastic modulus, Hybrid and NPR specimens had the highest and lowest ultimate strength, respectively. Moreover, the Hybrid specimens showed a higher plateau stress after yielding as compared to the PPR$_s$ and NPR specimens. This capability was more highlighted when the cellular forces largely deformed the structures. Such post-yield fluctuations of the stress-strain were mainly due to structural densifications caused by excessive deformation. In PPR$_p$, however, there was only a negligible degree of densification (Fig. 2a.ii and c). The maximum principal stress in all the structures occurred near the corners of the struts but with different distributions and magnitudes depending on the type of the structure. For instance, the maximum principal stress of PPR$_p$ was higher in the middle layer, unlike the NPR for which the maximum values occurred in the top and bottom layers. The distribution of the maximum principal stress in PPR$_s$ was more homogeneous than in the other groups.

Following the experimental and numerical results (Fig. 2d), the PPR structures, which are characterized by maximal effective elastic modulus ratios (PPR$_p$) and minimal effective elastic modulus ratios (PPR$_s$), experienced collapse under large deformation. The discrepancy between the experimental and FEM patterns for the PPR$_p$ and PPR$_s$ groups can be attributed to the inability of our FEM model to detect damage (or failure [57]) and collapse in the struts.

4.3. Cell-induced deformation of the meta-biomaterials

The fact that the local bending was more pronounced in the NPR meta-biomaterials can be attributed to the larger length of the struts (h) in this group, resulting in increased bending deformation. In contrast, the ZPR group, consisting of straight struts, demonstrated greater resistance to local bending. This may explain the fewer number of cells observed in the NPR group as compared to the ZPR and PPR$_p$ groups.

Furthermore, from a geometrical perspective, the NPR meta-biomaterial exhibits a negative and acute angle between the struts (*i.e.*, $\theta < 0$), whereas the ZPR and PPR$_p$ structures are characterized by zero or positive angles (*i.e.*, $\theta \geq 0$). Such sharp and negative angles in the unit cell of the NPR group may decrease cell growth as compared to the other groups. However, this requires further experiments and dedicated data analysis. Additionally, a noticeable graded bending of the struts was observed, specifically in the NPR group on day 8 (Figure S2 of the supplementary document). This suggests that prior to day 17, when the meta-biomaterial was not yet entirely covered by the cells, the first layer of the meta-biomaterial (particularly in the NPR group) was subjected to bending, resulting in the top surface deforming less (*i.e.*, smaller localized bending) (Figure S2 of the supplementary document).

The higher shrinkage in the PPR$_p$ group can be attributed to the increased E_L/E_T value in the PPR$_p$ group. A higher E_L/E_T value implies that while the PPR$_p$ group exhibited a greater longitudinal effective elastic modulus, it possessed a substantially lower effective elastic modulus in the transverse direction than the longitudinal one, leading to diminished mechanical strength in the transverse direction (Fig. 1d.ii and Table 1). Consequently, cells can more readily deform these structures (Fig. 3). Therefore, the volumetric contraction was more pronounced in the PPR$_p$ group, as compared to local bending.

The cell-induced shrinkage of the meta-biomaterials can be used to study some aspects of mechanotransduction in bone cells. The force transmitted from the cell nuclei to focal adhesion and then to the meta-biomaterials can be back-calculated using computational models [58]. This type of analysis, which is based on computational modeling of some aspects of the relevant mechanobiological processes, can offer a tool for indirect measurement of cellular forces [59,60].

The shrinkage of the non-seeded specimens (Fig. 3, first column) was attributed to the properties of the IP-Q material and the micro-architectures of the designed meta-biomaterials. Capillary forces during the fixation and dehydration of the specimens caused them to shrink. In the case of the PPR$_p$ group, higher shrinkage was observed due to the greater differences in its longitudinal and transverse effective elastic moduli (Fig. 1d.ii).

4.4. Metabolic activity and osteogenic response of the preosteoblast cells

The reduced metabolic activity in the NPR group is likely due to the sharp angles in the NPR specimens as compared to the positive Poisson's ratio structures, which probably hindered cellular adaptation to this micro-architecture, as suggested by the SEM images (Fig. 3, day 10 and S2 of the supplementary document, days 8, 13). This may have adversely affected cell growth. Surprisingly, our findings contrast with the reports available in the literature suggesting that auxeticity provides a more favorable environment for mesenchymal stem cells growth [17]. Such contradictory results warrant further investigation for clarification. These discrepancies may be due to the improved isolation of the Poisson's ratio from other micro-architectural parameters in this study as compared to other studies, as well as due to the different cell types, unit cell types and material used. Furthermore, although cells managed to reach and cover most of the meta-biomaterials after 17 days of culture, cell-free spaces remained visible. This observation was supported by the increasing metabolic activity measured until day 17 and higher magnification SEM images (Fig. 4 and S2 of the supplementary document).

Regarding the osteogenic response of the preosteoblast cells in the meta-biomaterials, no significant differences in the expression of Runx2 were detected among the various groups (Fig. 5b.i). However, the expressions of both Runx2 and ARS were non-significantly higher in the NPR group as compared to the PPR one (Fig. 5b.i and ii). Previous studies have shown that the neural differentiation of pluripotent stem cells may be higher in positive Poisson's ratio scaffolds as compared to auxetic scaffolds [9]. These findings confirm that the scaffolds were able to support the osteogenic differentiation of preosteoblasts and matrix mineralization. Further research is required to fully understand the effects of the Poisson's ratio on these cellular functions. However, the unit cell geometry appears to influence cell growth in these structures, warranting additional exploration.

It is worth mentioning that different types of ordered or disordered (*i.e.*, random) meta-biomaterials [61] can be designed with the same Poisson's ratios. It is entirely possible and, indeed, likely that cells respond differently to distinct unit cell designs, even if

the structures maintain an identical Poisson's ratio. This aspect was a central focus of our study, where we observed different cell behaviors with the ZPR and Hybrid meta-biomaterials, despite both exhibiting almost similar values of the Poisson's ratio.

It should be also noted that while we studied the response of cells to the designed meta-biomaterials under static culture conditions, the cells themselves deformed the meta-biomaterials significantly over a 17-day culture duration (Fig. 3). It is, however, important to study the effects of external, dynamic loading on the cell response of meta-biomaterials. Introducing dynamic loading conditions can add complexities, such as changes in the movement of the medium, temporal changes in the pore size, differences in the structure of the unit cell, and local cellular deformations. These factors might influence the cell behavior and need to be further studied in the future. Here we used the cell seeding along the *y*-direction. We believe that the direction of cell seeding might also influence the cell responses (*e.g.,* cell proliferation and differentiation) due to variations in the unit cell configurations and their mechanical properties.

5. Conclusions

We studied the influence of the Poisson's ratio of 3D meta-biomaterials on the behavior of preosteoblast cells. Therefore, we initially used computational models to rationally design 3D meta-biomaterials. In this design, the Poisson's ratio was isolated from other micro-architectural parameters and mechanical properties, such as the effective elastic modulus, porosity, and pore size. For the fabrication of these complex meta-biomaterials at the meso–scale, we used an advanced micro-AM technique (*i.e.,* 2PP) and IP-Q as the base material. Both the micro- and meso–mechanical characterizations of the IP-Q and meta-biomaterials showed a high degree of material nonlinearity (*i.e.,* hyperelastic behavior). The hyperelastic behavior of the polymerized IP-Q photoresist was modeled using the third-order reduced polynomial model. We designed the final meta-biomaterials using an FEM approach, considering the hyperelastic properties of the polymerized IP-Q, porosity of the trabecular bone, and the size of preosteoblasts. The cell-laden meta-biomaterials exhibited differences in terms of cell infiltration along the struts, (lateral) structural deformation over time, and metabolic activity of the cells. The cells seeded on the meta-biomaterials with positive values of the Poisson's ratio (*i.e.,* v_{yz}) demonstrated significantly higher levels of metabolic activity and induced more deformation of the structures as compared to those seeded on the meta-biomaterials with negative values of the Poisson's ratio. This difference in the cell responses is likely due to the unit cell geometry and anisotropy in the effective elastic modulus, with the PPR$_P$ having the most pronounced anisotropy, leading to increased deformation.

Furthermore, all the meta-biomaterials considered here supported the osteogenic differentiation of preosteoblasts as well as matrix mineralization even though there were no significant differences between the various groups. In summary, this study presents a new platform for the design, fabrication, and assessment of meso–scale meta-biomaterials with controlled Poisson's ratios. The presented design approach also holds considerable promise for the development of bone implants and may contribute toward expanding our understanding of how physical cues impact cell responses, both individually and in combination.

Declaration of competing interest

The authors declare that they have no known competing financial interests or personal relationships that could have appeared to influence the work reported in this paper.

Funding

Supplementary materials

Supplementary material associated with this article can be found, in the online version, at doi:10.1016/j.actbio.2024.01.045.

References

[1] B. Yi, Q. Xu, W. Liu, An overview of substrate stiffness guided cellular response and its applications in tissue regeneration, Bioact. Mater (2021).

[2] A. Maggi, H. Li, J.R. Greer, Three-dimensional nano-architected scaffolds with tunable stiffness for efficient bone tissue growth, Acta Biomater. 63 (2017) 294–305.

[3] T. Jiang, X.-Y. Tang, Y. Mao, Y.-Q. Zhou, J.-J. Wang, R.-M. Li, X.-R. Xie, H.-M. Zhang, B. Fang, N.-J. Ouyang, Matrix mechanics regulate the polarization state of bone marrow-derived neutrophils through the JAK1/STAT3 signaling pathway, Acta Biomater. (2023).

[4] A. Vilar, M. Hodgson-Garms, G.D. Kusuma, I. Donderwinkel, J. Carthew, J.L. Tan, R. Lim, J.E. Frith, Substrate mechanical properties bias MSC paracrine activity and therapeutic potential, Acta Biomater. (2023).

[5] A. Bizanti, P. Chandrashekar, R. Steward Jr, Culturing astrocytes on substrates that mimic brain tumors promotes enhanced mechanical forces, Exp. Cell Res. 406 (2) (2021) 112751.

[6] L.C. Ransanz, P.F. Van Altena, V.M. Heine, A. Accardo, Engineered cell culture microenvironments for mechanobiology studies of brain neural cells, Front. Bioeng. Biotechnol. 10 (2022) 1096054.

[7] A. Accardo, C. Cirillo, S. Lionnet, C. Vieu, I. Loubinoux, Interfacing cells with microengineered scaffolds for neural tissue reconstruction, Brain Res. Bull. 152 (2019) 202–211.

[8] M. Niinomi, M. Nakai, Titanium-based biomaterials for preventing stress shielding between implant devices and bone, Int. J. Biomater. 2011 (2011).

[9] Y. Yan, Y. Li, L. Song, C. Zeng, Pluripotent stem cell expansion and neural differentiation in 3-D scaffolds of tunable Poisson's ratio, Acta Biomater. 49 (2017) 192–203.

[10] B. Zou, Z. Liang, D. Zhong, Z. Cui, K. Xiao, S. Shao, J. Ju, Magneto-thermo-mechanically reprogrammable mechanical metamaterials, Adv. Mater. 35 (8) (2023) 2207349.

[11] M.E. Pallarès, I. Pi-Jaumà, I.C. Fortunato, V. Grazu, M. Gómez-González, P. Roca-Cusachs, J.M. de la Fuente, R. Alert, R. Sunyer, J. Casademunt, Stiffness-dependent active wetting enables optimal collective cell durotaxis, Nat. Phys. 19 (2) (2023) 279–289.

[12] P. Chansoria, J. Blackwell, E.L. Etter, E.E. Bonacquisti, N. Jasiewicz, T. Neal, S.A. Kamal, J. Hoque, S. Varghese, T. Egan, Rationally designed anisotropic and auxetic hydrogel patches for adaptation to dynamic organs, Adv. Funct. Mater. 32 (43) (2022) 2207590.

[13] E. Yarali, A.A. Zadpoor, U. Staufer, A. Accardo, M.J. Mirzaali, Auxeticity as a mechanobiological tool to create meta-biomaterials, ACS Appl. Bio Mater 6 (7) (2023) 2562–2575.

[14] H. Haag, P.D. Dalton, V. Bloemen, The synergy of biomimetic design strategies for tissue constructs, Adv. Funct. Mater. (2022) 2201414.

[15] N. Munding, M. Fladung, Y. Chen, M. Hippler, A.D. Ho, M. Wegener, M. Bastmeyer, M. Tanaka, Bio-metamaterials for mechano-regulation of mesenchymal stem cells, Adv. Funct. Mater. (2023) 2301133.

[16] G. Flamourakis, I. Spanos, Z. Vangelatos, P. Manganas, L. Papadimitriou, C. Grigoropoulos, A. Ranella, M. Farsari, Laser-made 3D auxetic metamaterial scaffolds for tissue engineering applications, Macromol. Mater. Eng. 305 (7) (2020) 2000238.

[17] A. Tang, J. Ji, J. Li, W. Liu, J. Wang, Q. Sun, Q. Li, Nanocellulose/PEGDA aerogels with tunable Poisson's ratio fabricated by stereolithography for mouse bone marrow mesenchymal stem cell culture, Nanomater 11 (3) (2021) 603.

[18] W. Lv, L. Dong, D. Li, A novel metamaterial with individually adjustable and sign-switchable Poisson's ratio, Eur. J. Mech. A/Solids 97 (2023) 104851.

[19] D. Li, J. Yin, L. Dong, R.S. Lakes, Strong re-entrant cellular structures with negative Poisson's ratio, J. Mater. Sci. 53 (5) (2018) 3493–3499.

[20] K.K. Dudek, J.A.I. Martínez, G. Ulliac, M. Kadic, Micro-scale auxetic hierarchical mechanical metamaterials for shape morphing, Adv. Mater. 34 (14) (2022) 2110115.

[21] X. Xin, L. Liu, Y. Liu, J. Leng, 4D printing auxetic metamaterials with tunable, programmable, and reconfigurable mechanical properties, Adv. Funct. Mater. 30 (43) (2020) 2004226.

[22] B. Jang, S. Won, J. Kim, J. Kim, M. Oh, H.J. Lee, J.H. Kim, Auxetic meta-display: stretchable display without image distortion, Adv. Funct. Mater. 32 (22) (2022) 2113299.

[23] D. Chen, D. Li, K. Pan, S. Gao, B. Wang, M. Sun, C. Zhao, X. Liu, N. Li, Strength enhancement and modulus modulation in auxetic meta-biomaterials produced by selective laser melting, Acta Biomater. 153 (2022) 596–613.

[24] Y. Zhu, S. Jiang, Q. Zhang, J. Li, C. Yu, C. Zhang, A novel monoclinic auxetic metamaterial with tunable mechanical properties, Int. J. Mech. Sci. 236 (2022) 107750.

[25] A. Sorrentino, D. Castagnetti, Novel polyhedral mechanical metamaterial exhibiting negative Poisson's ratio, Smart Mater. Struct. 32 (3) (2023) 035008.

[26] Y. Zhu, S. Jiang, J. Li, D.K. Pokkalla, Q. Wang, C. Zhang, Novel isotropic anti-tri-missing rib auxetics with prescribed in-plane mechanical properties over large deformations, Int. J. Appl. Mech. 13 (10) (2021) 2150115.

[27] W. Lv, D. Li, L. Dong, Study on blast resistance of a composite sandwich panel with isotropic foam core with negative Poisson's ratio, Int. J. Mech. Sci. 191 (2021) 106105.

[28] M.J. Mirzaali, A. Ghorbani, K. Nakatani, M. Nouri-Goushki, N. Tümer, S.J. Callens, S. Janbaz, A. Accardo, J. Bico, M. Habibi, A.A. Zadpoor, Curvature induced by deflection in thick meta-plates, Adv. Mater. 33 (30) (2021) 2008082.

[29] Y. Zhu, Y. Luo, D. Gao, C. Yu, X. Ren, C. Zhang, In-plane elastic properties of a novel re-entrant auxetic honeycomb with zigzag inclined ligaments, Eng. Struct. 268 (2022) 114788.

[30] M. Mirzaali, H. Pahlavani, E. Yarali, A. Zadpoor, Non-affinity in multi-material mechanical metamaterials, Sci. Rep. 10 (1) (2020) 11488.

[31] A. Sorrentino, D. Castagnetti, L. Mizzi, A. Spaggiari, Bio-inspired auxetic mechanical metamaterials evolved from rotating squares unit, Mech. Mater. 173 (2022) 104421.

[32] H.M. Kolken, S. Janbaz, S.M. Leeflang, K. Lietaert, H.H. Weinans, A.A. Zadpoor, Rationally designed meta-implants: a combination of auxetic and conventional meta-biomaterials, Mater. Horiz. 5 (1) (2018) 28–35.

[33] A. Sorrentino, D. Castagnetti, Negative Poisson's ratio lattice for designing vertebral biomaterials, Mech. Adv. Mater. Struct. 29 (27) (2022) 6626–6633.

[34] A.A. Zadpoor, M.J. Mirzaali, L. Valdevit, J.B. Hopkins, Design, material, function, and fabrication of metamaterials, APL. Mater. 11 (2) (2023).

[35] I. Ostanin, G. Ovchinnikov, D.C. Tozoni, D. Zorin, A parametric class of composites with a large achievable range of effective elastic properties, J. Mech. Phys. Solids. 118 (2018) 204–217.

[36] Z. Hashin, The Elastic Moduli of Heterogeneous Materials, US Department of Commerce, Office of Technical Services, 1960.

[37] Z. Hashin, S. Shtrikman, A variational approach to the theory of the elastic behaviour of multiphase materials, J. Mech. Phys. Solids. 11 (2) (1963) 127–140.

[38] W. Zhang, P. Soman, K. Meggs, X. Qu, S. Chen, Tuning the poisson's ratio of biomaterials for investigating cellular response, Adv. Funct. Mater. 23 (25) (2013) 3226–3232.

[39] J.W. Lee, P. Soman, J.H. Park, S. Chen, D.-W. Cho, A tubular biomaterial construct exhibiting a negative Poisson's ratio, PLoS. One 11 (5) (2016) e0155681.

[40] L. Song, M.F. Ahmed, Y. Li, C. Zeng, Y. Li, Vascular differentiation from pluripotent stem cells in 3-D auxetic scaffolds, Tissue Eng. Regen. Med. 12 (7) (2018) 1679–1689.

[41] A. Accardo, M.-C. Blatché, R. Courson, I. Loubinoux, C. Vieu, L. Malaquin, Direct laser fabrication of free-standing PEGDA-hydrogel scaffolds for neuronal cell growth, Mater Today 21 (3) (2018) 315–316.

[42] T. Abele, T. Messer, K. Jahnke, M. Hippler, M. Bastmeyer, M. Wegener, K. Göpfrich, Two-photon 3D laser printing inside synthetic cells, Adv. Mater. 34 (6) (2022) 2106709.

[43] C. Wang, Z. Vangelatos, C.P. Grigoropoulos, Z. Ma, Micro-engineered architected metamaterials for cell and tissue engineering, Mater. Today Adv. 13 (2022) 100206.

[44] J. Im, Y. Liu, Q. Hu, G.F. Trindade, C. Parmenter, M. Fay, Y. He, D.J. Irvine, C. Tuck, R.D. Wildman, Strategies for integrating metal nanoparticles with two-photon polymerization process: toward high resolution functional additive manufacturing, Adv. Funct. Mater. (2023) 2211920.

[45] V. Harinarayana, Y. Shin, Two-photon lithography for three-dimensional fabrication in micro/nanoscale regime: a comprehensive review, Opt. Laser. Technol. 142 (2021) 107180.

[46] N. Barin, H.E. Balcioglu, I. de Heer, M. de Wit, M.L. Lamfers, M.E. van Royen, P.J. French, A. Accardo, 3D-Engineered scaffolds to study microtubes and localization of epidermal growth factor receptor in patient-derived glioma cells, Small (2022) 2204485.

[47] A. Sharaf, B. Roos, R. Timmerman, G.-J. Kremers, J.J. Bajramovic, A. Accardo, Two-photon polymerization of 2.5 D and 3D microstructures fostering a ramified resting phenotype in primary microglia, Front. Bioeng. Biotechnol. 10 (2022) 926642.

[48] Q. Akolawala, M. Rovituso, H.H. Versteeg, A.M. Rondon, A. Accardo, Evaluation of proton-induced DNA damage in 3D-engineered glioblastoma microenvironments, ACS Appl. Mater. Interfaces 14 (18) (2022) 20778–20789.

[49] T. Wang, H. Ugurlu, Y. Yan, M. Li, M. Li, A.-M. Wild, E. Yildiz, M. Schneider, D. Sheehan, W. Hu, Adaptive wireless millirobotic locomotion into distal vasculature, Nat. Commun. 13 (1) (2022) 4465.

[50] S. Chen, Z. Tan, P. Liao, Y. Li, Y. Qu, Q. Zhang, M. Yang, K.W.Y. Chan, L. Zhang, K. Man, Biodegradable microrobots for DNA vaccine delivery, Adv. Healthc. Mater (2023) 2202921.

[51] I.J. Gibson, M.F. Ashby, The mechanics of three-dimensional cellular materials, Proc. Math. Phys. Eng. Sci. 382 (1782) (1982) 43–59.

[52] V. Karageorgiou, D. Kaplan, Porosity of 3D biomaterial scaffolds and osteogenesis, Biomater 26 (27) (2005) 5474–5491.

[53] R. Hedayati, M. Sadighi, M. Mohammadi-Aghdam, A. Zadpoor, Effect of mass multiple counting on the elastic properties of open-cell regular porous biomaterials, Mater. Des. 89 (2016) 9–20.

[54] J. Cohen, Eta-squared and partial eta-squared in fixed factor ANOVA designs, Educ. Psychol. Meas. 33 (1) (1973) 107–112.

[55] J. Cohen, Statistical Power Analysis for the Behavioral Sciences, Academic Press, 2013.

[56] Q. Hu, G.A. Rance, G.F. Trindade, D. Pervan, L. Jiang, A. Foerster, L. Turyanska, C. Tuck, D.J. Irvine, R. Hague, The influence of printing parameters on multi-material two-photon polymerisation based micro additive manufacturing, Addit. Manuf. 51 (2022) 102575.

[57] J. Fortin-Smith, J. Sherwood, P. Drane, D. Kretschmann, Characterization of maple and ash material properties for the finite element modeling of wood baseball bats, Appl. Sci. 8 (11) (2018) 2256.

[58] J. Barrasa-Fano, A. Shapeti, A. Jorge-Penas, M. Barzegari, J.A. Sanz-Herrera, H. Van Oosterwyck, TFMLAB: a MATLAB toolbox for 4D traction force microscopy, SoftwareX. 15 (2021) 100723.

[59] A.D. Lantada, A. Muslija, J.P. García-Ruíz, Auxetic tissue engineering scaffolds with nanometric features and resonances in the megahertz range, Smart. Mater. Struct. 24 (5) (2015) 055013.

[60] D.O. Sohutskay, A.B. Tepole, S.L. Voytik-Harbin, Mechanobiological wound model for improved design and evaluation of collagen dermal replacement scaffolds, Acta Biomater. 135 (2021) 368–382.

[61] M.J. Mirzaali, V. Moosabeiki, S.M. Rajaai, J. Zhou, A.A. Zadpoor, Additive manufacturing of biomaterials—design principles and their implementation, Materials 15 (15) (2022) 5457.